

Hyperactive mTORC1 in lung mesenchyme induces endothelial cell dysfunction and pulmonary vascular remodeling

Susan M. Lin, ... , Jillian F. Evans, Vera P. Krymskaya

J Clin Invest. 2023. <https://doi.org/10.1172/JCI172116>.

Research

In-Press Preview

Cell biology

Vascular biology

Lymphangioleiomyomatosis (LAM) is a progressive cystic lung disease caused by *tuberous sclerosis complex 1/2* (*TSC1/2*) gene mutations in pulmonary mesenchymal cells resulting in activation of the mechanistic target of rapamycin complex 1 (mTORC1). A subset of LAM patients develops pulmonary vascular remodeling and pulmonary hypertension. Little, however, is known regarding how LAM cells communicate with endothelial cells (ECs) to trigger vascular remodeling. In end-stage LAM lung explants, we identified endothelial cell dysfunction characterized by increased proliferation, migration, defective angiogenesis, and dysmorphic endothelial tube network formation. To model LAM disease, we utilized an mTORC1 gain-of-function mouse model with a *Tsc2* knock-out (*Tsc2^{KO}*) specific to lung mesenchyme (*Tbx4^{LME-Cre}Tsc2^{fl/fl}*), similar to the mesenchyme specific genetic alterations seen in human disease. As early as 8 weeks of age, ECs from *Tbx4^{LME-Cre}Tsc2^{fl/fl}* mice exhibited marked transcriptomic changes despite absence of morphological changes to the distal lung microvasculature. In contrast, 1 year old *Tbx4^{LME-Cre}Tsc2^{fl/fl}* mice spontaneously developed pulmonary vascular remodeling with increased medial thickness. Single cell RNA-sequencing of 1 year old mouse lung identified paracrine ligands originating from *Tsc2^{KO}* mesenchyme which can signal through receptors in arterial ECs. These ECs had transcriptionally altered genes including those in pathways associated with blood vessel remodeling. The proposed pathophysiologic mesenchymal ligand/ EC receptor crosstalk highlights the importance of an altered mesenchymal-EC axis in LAM and other hyperactive mTORC1-driven diseases. [...]

Find the latest version:

<https://jci.me/172116/pdf>



Hyperactive mTORC1 in Lung Mesenchyme Induces Endothelial Cell Dysfunction and Pulmonary Vascular Remodeling

Susan M. Lin^{1,2}, Ryan Rue¹, Alexander R. Mukhitov¹, Akansha Goel¹, Maria C. Basil^{1,2,3}, Kseniya Obraztsova¹, Apoorva Babu², Slaven Crnkovic^{4,6}, Owen Ledwell¹, Laura T. Ferguson^{1,2}, Joseph D. Planer^{1,2}, Ana N. Nottingham^{1,2}, Kanth Swaroop Vanka¹, Carly J. Smith¹, Edward Cantu III^{2,7}, Grazyna Kwapiszewska^{4,6}, Edward E. Morrisey^{2,3}, Jillian F. Evans¹, and Vera P. Krymskaya^{1,2*}

¹ Division of Pulmonary, Allergy, and Critical Care Medicine, Department of Medicine, Perelman School of Medicine, University of Pennsylvania, Philadelphia, PA, USA.

² Lung Biology Institute, University of Pennsylvania, Philadelphia, PA, USA.

³ Penn Cardiovascular Institute, University of Pennsylvania, Philadelphia, PA, USA

⁴ Division of Physiology, Medical University of Graz, Graz, Austria.

⁵ Ludwig Boltzmann Institute for Lung Vascular Research, Graz, Austria.

⁶ Institute for Lung Health, Justus Liebig University Giessen Germany, Giessen, Germany.

⁷ Department of Surgery, Perelman School of Medicine, University of Pennsylvania, Philadelphia, PA, USA.

The authors have declared that no conflict of interest exists.

Abstract

Lymphangioleiomyomatosis (LAM) is a progressive cystic lung disease caused by *tuberous sclerosis complex 1/2 (TSC1/2)* gene mutations in pulmonary mesenchymal cells resulting in activation of the mechanistic target of rapamycin complex 1 (mTORC1). A subset of LAM patients develops pulmonary vascular remodeling and pulmonary hypertension. Little, however, is known regarding how LAM cells communicate with endothelial cells (ECs) to trigger vascular remodeling. In end-stage LAM lung explants, we identified endothelial cell dysfunction characterized by increased proliferation, migration, defective angiogenesis, and dysmorphic endothelial tube network formation. To model LAM disease, we utilized an mTORC1 gain-of-function mouse model with a *Tsc2* knock-out (*Tsc2^{KO}*) specific to lung mesenchyme (*Tbx4^{LME-Cre}Tsc2^{fl/fl}*), similar to the mesenchyme specific genetic alterations seen in human disease. As early as 8 weeks of age, ECs from *Tbx4^{LME-Cre}Tsc2^{fl/fl}* mice exhibited marked transcriptomic changes despite absence of morphological changes to the distal lung microvasculature. In contrast, 1 year old *Tbx4^{LME-Cre}Tsc2^{fl/fl}* mice spontaneously developed pulmonary vascular remodeling with increased medial thickness. Single cell RNA-sequencing of 1 year old mouse lung identified paracrine ligands originating from *Tsc2^{KO}* mesenchyme which can signal through receptors in arterial ECs. These ECs had transcriptionally altered genes including those in pathways associated with blood vessel remodeling. The proposed pathophysiologic mesenchymal ligand/ EC receptor crosstalk highlights the importance of an altered mesenchymal-EC axis in LAM and other hyperactive mTORC1-driven diseases. Since ECs in LAM patients and in *Tbx4^{LME-Cre}Tsc2^{fl/fl}* mice do not harbor *TSC2* mutations, our study demonstrates that constitutively active mTORC1 lung mesenchymal cells orchestrate dysfunctional EC responses which contribute to pulmonary vascular remodeling.

Introduction

Lymphangioleiomyomatosis (LAM) is a destructive lung disease characterized by diffuse parenchymal cystic airspace enlargement, airflow obstruction, and chylothorax from lymphatic involvement (1-6). In addition, some LAM patients develop pulmonary vascular remodeling with intimal and medial hypertrophy of pulmonary arteries (7) and subsequent pulmonary hypertension (7-9). There are two forms of LAM: sporadic and inherited. Both sporadic and inherited LAM result from loss-of-function mutations in the *tuberous sclerosis complex 1/2* (*TSC1/TSC2*) genes resulting in constitutive activation of the mechanistic target of rapamycin (mTOR) pathway, specifically mTOR complex 1 (mTORC1) (10-12). This genetic mutation only occurs in a distinct population of mesenchymal cells known as “LAM cells” (13). LAM cells, which been estimated to be less than 5% of the total lung cell population, are localized in the pulmonary parenchyma adjacent to cystic lesions, bronchioles, vasculature, and lymphatics (7). Pulmonary lesions formed by LAM cells consist of mixed mesenchymal populations with myofibroblast-like spindle-shaped cells expressing smooth muscle-specific markers and epithelioid-like cells expressing glycoprotein gp100 (5).

Single cell RNA sequencing (scRNA-seq) of LAM lungs has shown marked transcriptomic changes in cell populations surrounding LAM cell lesions, including mesenchymal and epithelial cells (14). The effect of aberrant mTOR signaling in LAM cells on endothelial cells (ECs) and pulmonary vasculature has not been previously investigated. Thus, it is unknown how LAM cells, localized in the lung interstitium, alter the behavior and function of vascular ECs. The role of mTOR hyperactivation on the LAM mesenchymal-EC cell axis is particularly significant as mTOR pathway activation has been recently implicated in the progression of pulmonary vascular remodeling in pulmonary hypertension (PH) (15-19). Prior research has demonstrated that mTORC2-dependent activation of mTORC1 through oxidative stress is a major cause of vascular remodeling by coordinating pulmonary artery smooth muscle cell (PASMC) metabolism and proliferation (15). Follow up studies have identified mTORC1 as a mediator of PASMC function under hypoxic conditions (20) and in pathogenic right ventricular remodeling (21). More recently, smooth muscle cell-specific conditional knockouts of *Raptor* or *Rictor* in murine models

found that inhibition of mTORC1 attenuates the development of PH while inhibition of mTORC2 caused spontaneous PH (19).

To better understand the role of mTORC1 activation in mesenchymal cells on lung EC dysfunction and pulmonary vascular remodeling, we generated primary cultures of ECs from human LAM patients and demonstrated that dysregulated WNT signaling in mTORC1 hyperactive mesenchymal cells contributes to EC dysfunction. To further investigate how mesenchymal cells alter EC behavior, we generated a murine model with selective *Tsc2* deletion in pulmonary mesenchymal progenitors (*Tbx4*^{LME-Cre}*Tsc2*^{fl/fl}) (14). We previously found that *Tbx4*^{LME-Cre}*Tsc2*^{fl/fl} mice with mesenchyme-specific loss of *Tsc2* developed age- and sex-dependent decline in pulmonary function and destruction of alveolar lung structure (14). In this study, we focused on the effects of the mutated lung mesenchyme on pulmonary ECs and found changes in EC function and transcriptomic signature. Moreover, parallel to the development of PH in a subset of patients with late-stage LAM, aged *Tbx4*^{LME-Cre}*Tsc2*^{fl/fl} mice spontaneously developed pulmonary vascular remodeling with concurrent elevation in right ventricular systolic pressure. Taken together, our novel research demonstrates that mTORC1 hyperactivation in lung mesenchyme causes vascular EC dysfunction through proliferation and phenotypic transformation of pulmonary artery ECs. This aberrant signaling response subsequently results in pulmonary vascular remodeling and further emphasizes the pathogenic importance of the mesenchymal-EC communication axis as a potential cause of pulmonary vascular remodeling.

Results

ECs from LAM lung explants are characterized by a hyperproliferative phenotype with reduced angiogenic capacity in 2-dimensional (2D) monoculture.

To elucidate the possibility of vascular EC dysfunction in LAM, we performed histopathological analysis on diseased lung explants obtained from LAM patients at the time of lung transplantation. End-stage LAM lung explants exhibit diffuse parenchymal cysts (not shown; for overview of LAM as cystic lung disease see Koslow *et al.* 2023 (22)), lymphatic involvement, as well as remodeled vessels (Fig 1A) with concentric fibrosis of the intima and media (Fig 1B). Interspersed in the lung parenchyma are LAM

micronodules consisting of mesenchymal LAM cells which stain positive for phosphorylated ribosomal protein S6 (pS6), a marker of mTORC1 activation (12) (Fig 1C). LAM cells of mesenchymal origin are the only cell types in the LAM lung to harbor *TSC2* mutations, while pulmonary cells of other lineages, including ECs, do not harbor *TSC2* mutations. As such, ECs from both control and LAM lungs have *TSC2* expression detected by dual immunohistochemistry (Fig 1D) and RNAscope (Supplemental Fig 1A).

To purify and characterize ECs, LAM lung specimens with distal pulmonary vasculature were mechanically dissected and enzymatically dissociated into single cell suspensions as previously described (23, 24). To ensure capture of distal cells, only peripheral lung segments, identified by presence of visceral pleura, were utilized. Micro-dissection was performed along the broncho-vascular bundle, and vascular ECs were isolated using antibody-magnetic bead sorting and grown to confluence on fibronectin-coated plates (Supplemental Fig 1B). To confirm cell-type identity and purity, we examined expression patterns on flow cytometry with canonical lineage markers (CD45 for immune populations, EPCAM for epithelial populations, and CD31 for endothelial populations; Supplemental Fig 1C). Immunoblot of primary fibroblasts derived from LAM lung was notable for a significant decrease in *TSC2* expression (Supplemental Fig 1D) while there were no significant differences in *TSC2* protein expression in purified ECs isolated from LAM compared to control lungs (Supplemental Fig 1E). Control pulmonary vascular ECs exhibited a polygonal morphology with an organized cobblestone appearance. Compared to age- and sex-matched controls, LAM-derived ECs were dysmorphic, hypertrophic, and less uniform in appearance with increased randomly oriented actin fibers (Fig 1E).

Similar to existing studies of ECs isolated from remodeled PH vasculature (25, 26), we found that LAM ECs were more proliferative (Fig 1F) with increased migration (Fig 1G-H), but reduced angiogenic capacity as measured by in vitro tube formation assay (Fig 1I). On these 2-D monocultures, LAM ECs exhibited decreased tube lengths compared to control ECs, indicating reduced angiogenic potential when grown in the absence of support cells (Fig 1J).

LAM lung fibroblasts increase angiogenic potential of LAM ECs.

As vascular ECs from LAM lungs do not harbor *TSC1* or *TSC2* mutations and do not have any previously known roles in LAM pathogenesis, it is unclear how mesenchymal LAM cells with constitutive mTORC1 hyperactivation altered vascular EC function. We speculated that this could occur through paracrine signaling between mesenchymal and vascular ECs. Thus, to assess EC-mesenchymal crosstalk through cell-cell and cell-matrix interactions, primary ECs and fibroblasts from LAM patients or control human lung were co-cultured in 2D on fibronectin-coated 12-well plates (Fig 2A). In 2D cocultures with LAM fibroblasts, ECs from LAM lung demonstrated a very different morphology with increased affinity for self-segregation and self-organization (Fig 2B). To investigate how EC behavior is altered by surrounding cells and the pulmonary microenvironment, we developed EC-fibroblast cocultures to interrogate cell-cell interactions and 3-dimensional (3D) EC-fibroblast cocultures to investigate cell-matrix interactions. First, ECs from LAM lungs were more proliferative than control ECs when cocultured with control fibroblasts, which increased further when ECs from LAM lung were cocultured with LAM fibroblasts (Fig 2C). Thus, LAM fibroblasts appear to have an additive effect on LAM EC growth and proliferation. Next, the ability of ECs from LAM lung to self-assemble and form endothelial tubes was assessed within 3D extracellular matrix (ECM)-based scaffolds (Fig 2D). When ECs were grown as a monoculture in 3D sphericals, there was a trend towards increased EC proliferation, but a non-significant difference in total tube length and cell count between ECs from LAM lung and control human ECs (Fig 2E). However, when grown in coculture with LAM lung-derived fibroblasts, ECs from LAM lung developed more extensive tube networks (Fig 2F) with increased EC proliferation (Fig 2G). Taken together, the major changes in EC organization in 2D cocultures and the significant increase in cell count and tube formation in 3D cocultures suggest that mesenchymal cells from LAM lung induce EC proliferation and in vitro vasculogenesis.

LAM scRNA-seq reveals transcriptomic alterations in pulmonary vascular ECs.

To assess the gene expression profile in LAM ECs, we analyzed LAM scRNA-seq data of LAM lung mesenchymal and EC clusters. Epithelial, immune, mesenchymal, and ECs were identified using

canonical markers (27-30). ECs were subsequently subclassified for further analysis based on EC-selective markers (27, 31). Pulmonary arterial ECs were characterized by high expression of *GJA5* and *DKK2* genes; venous ECs by *ACKR1* and *HDAC9*; lymphatic ECs by *PROX1*, capillary (CAP) ECs by *ILJR* (CAP1) or *EDNRB* (CAP2); and Car4-high (Car4⁺) ECs by *CA4* and *CD34*.

In this analysis, we found increased WNT2 ligand expression in two mesenchymal populations in the LAM lung: mesenchymal alveolar niche cells (MANC) (32) and unique LAM cells (Fig 3A). We also observed expression of the cognate WNT2 receptor, Frizzled 4 (FZD), in LAM ECs (Fig 3A). Since activation of both canonical and non-canonical WNT signaling pathways play a key role in the preservation of pulmonary vascular homeostasis (33), the presence of WNT activation in LAM mesenchymal cells was confirmed by in situ hybridization with RNAscope of the WNT pathway marker, AXIN2 (Supplemental Fig 2A). In particular, WNT2 mRNA was significantly increased in LAM lung fibroblasts compared to normal human lung fibroblasts by RNAscope of WNT2 (Fig 3B-C). This was further validated by qPCR for WNT2 in LAM lung fibroblasts compared to control fibroblasts (Fig 3D).

WNT2 activation of control ECs recapitulated LAM EC morphology.

To assess the effect of WNT pathway inhibition on in vitro EC function, LAM ECs were treated with C82, a WNT/ β -catenin pathway transcriptional inhibitor that disrupts the interaction between cyclic AMP response element-binding protein (CBP)/ β -catenin (34, 35). C82 inhibition decreased EC proliferation (Fig 4A), migration (Fig 4B-C), and EC tube formation (Fig 4D-E). LAM EC cocultures were more susceptible to mTORC1 inhibition than control EC cocultures, but there was no significant difference in response to WNT inhibition (Fig 4F).

When control human ECs cocultured with control human fibroblasts were treated with WNT activators (CHIR99021 or the WNT2 ligand), there was a change in morphology that recapitulated the LAM EC phenotype and morphology (Fig 4G as compared to Fig 2B). In addition, there was an increase in EC cell number (Fig 4H). Taken together, these experiments demonstrate the ability of control human ECs to adopt LAM EC morphology following WNT pathway activation.

Loss of *Tsc2* in mouse lung mesenchyme caused transcriptomic alterations in ECs.

Our data from human LAM samples suggests that the mesenchymal LAM cells secrete increased WNT ligands, which may have subsequent effects on adjacent ECs. To test this hypothesis, we utilized our previously characterized and published *Tbx4*^{LME-Cre}*Tsc2*^{fl/fl} mice (14), a model of mTORC1 hyperactivation with targeted *Tsc2* deletion in lung mesenchymal cells (36). mTORC1 activation was confirmed by increased pS6 in pulmonary mesenchymal cells from *Tbx4*^{LME-Cre}*Tsc2*^{KO} versus *Tbx4*^{LME-Cre}*Tsc2*^{WT} mice (Fig 5A). Analogous to human LAM disease, cells of mesenchymal lineages in the *Tbx4*^{LME-Cre}*Tsc2*^{KO} exhibit significant loss of *Tsc2* expression with concurrent hyperactivation of mTORC1 detected with pS6 antibody (Fig 5B-C). Likewise, ECs from *Tbx4*^{LME-Cre}*Tsc2*^{KO} mouse lung express *Tsc2* at levels comparable to ECs from *Tbx4*^{LME-Cre}*Tsc2*^{WT} mice (Fig 5D-E). We performed bulk RNA sequencing in 8-week-old mice to characterize potential transcriptomic alterations in cellular lineages. Pulmonary ECs from *Tbx4*^{LME-Cre}*Tsc2*^{KO} mice showed marked upregulation in metabolic, growth, and angiogenic pathways compared to lung ECs from *Tbx4*^{LME-Cre}*Tsc2*^{WT} mice (Fig 5F). Analysis of the top differentially expressed genes in *Tbx4*^{LME-Cre}*Tsc2*^{KO} pulmonary ECs exhibited upregulation of WNT ligands and amplifiers including *Axin2* and WNT receptors *Fzd1*, *Fzd2*, *Fzd7* and *Fzd8* (Fig 5G). The upregulation of WNT ligands and amplifiers in ECs from *Tbx4*^{LME-Cre}*Tsc2*^{KO} mice demonstrates activation of WNT pathway via cross-talk from mTORC1-activated mesenchymal cells.

The transcriptome of pulmonary arterial ECs was significantly altered by WNT signals from mesenchymal cells.

We collected and analyzed scRNA-seq data from one-year-old *Tbx4*^{LME-Cre}*Tsc2*^{WT} and *Tbx4*^{LME-Cre}*Tsc2*^{KO} mice (Fig 6A). We subclustered EC populations expressing the pan-EC marker *Pecam1* (Fig 6B) and mesenchymal populations expressing markers *Pdgfra*, *Pdgfrβ* and *Msln* (Fig 6C). Amongst cells expressing the pan-EC marker *Pecam1*, further clustering generated previously described endothelial subpopulations including arterial endothelial cells (arterial ECs), venous endothelial cell (venous ECs), lymphatic endothelial cell (lymphatic ECs), capillary type 1 (CAP1 or general capillary), and capillary type 2 (CAP2 or aerocyte) (Fig 6D). To determine which EC populations are most altered,

we performed differential gene expression analysis and gene ontology (GO analysis) comparing each of the EC subpopulations. Compared to other EC populations, arterial ECs were the most transcriptionally altered with upregulation of pathways associated with vasculogenesis/vasculature development, angiogenesis, EC differentiation, EC proliferation and blood vessel remodeling (Fig 6E). *Bmp4*, *Pparg*, and *Sox17*, associated with vascular remodeling in PH, were among the genes with the highest differential differences in arterial ECs (Fig 6F). We used CellChat to analyze communication between arterial ECs and each of the mesenchymal populations. The top identified interactions included Wnt pathway genes (Supplemental Fig 3) with paracrine signals to arterial ECs from 3 mesenchymal populations including (1) Axin2 myofibrogenic progenitors (AMPs), (2) Wnt2-Pdgfra cells and (3) mesothelial cells; (Fig 6G). In situ hybridization of *Tbx4*^{LME-Cre}*Tsc2*^{KO} lungs were notable for concurrent mTORC1 and WNT pathway activation with increased Axin2 mRNA and pS6 (Fig 6H-I). In addition, there was increased Wnt2 mRNA on in situ hybridization of *Tbx4*^{LME-Cre}*Tsc2*^{KO} compared to *Tbx4*^{LME-Cre}*Tsc2*^{WT} vessels (Figure J-K).

mTORC1 activation selectively in lung mesenchymal cells results in pulmonary vascular remodeling, elevated right ventricular systolic pressure and hypertrophy in one-year-old *Tbx4*^{LME-Cre}*Tsc2*^{KO} mice.

Targeted mesenchymal *Tsc2* deletion altered EC angiogenesis but there were no significant effects on vessel number or peripheral muscularization at 12-, 16- and 20- weeks of age (Supplemental Fig 4A-B). However, the time to complete tube formation was significantly decreased in 8-week-old *Tbx4*^{LME-Cre}*Tsc2*^{KO} ECs (Supplemental Fig 4C). These results indicate that while there were no histopathological changes at younger ages, ECs isolated from young *Tbx4*^{LME-Cre}*Tsc2*^{KO} mice were functionally altered by the exposure to constitutively activated mTORC1 in the pulmonary mesenchyme.

To determine whether prolonged exposure to *Tsc2*^{KO} mesenchyme would further alter EC function and vascular morphology, pulmonary vasculature was reassessed in 54-week-old mice. Analyses of 54-week-old *Tbx4*^{LME-Cre}*Tsc2*^{KO} lungs (Fig 7A) demonstrated significant vascular remodeling compared to age-matched *Tbx4*^{LME-Cre}*Tsc2*^{WT} controls (Fig 7B-C). This was characterized by an increase in fully

muscularized vessels with subsequent decrease of non-muscularized vessels, confirmed using manual counts of selective immunohistochemical staining of vessels (Fig 7B) and an automated analysis using a program that identifies vessels and calculates degree of peripheral vascularization (Visiomorph); (Fig 7C). In addition, pulmonary vessels in *Tbx4^{LME-Cre}Tsc2^{KO}* mice had thicker medial walls (Fig 7D; Supplemental Fig 5), however, there were no differences in the total number of vessels (Fig 7E). We investigated right ventricular systolic pressures in 54-week-old mice by right heart catheterization and found elevated ventricular pressures in *Tbx4^{LME-Cre}Tsc2^{KO}* compared to *Tbx4^{LME-Cre}Tsc2^{WT}* (Fig 7F). *Tbx4^{LME-Cre}Tsc2^{KO}* also had larger hearts measured by gross weight (Fig 7G), with higher right ventricular mass as measured by Fulton Index (Fig 7H). Fulton Index, a metric of right ventricular hypertrophy, which was most notable in female *Tbx4^{LME-Cre}Tsc2^{KO}* mice (Fig 7I). These findings were not present at younger ages (Supplemental Fig 6). Taken together, these findings demonstrated that mesenchymal mTORC1 activation resulted in spontaneous vascular remodeling in one-year-old *Tbx4^{LME-Cre}Tsc2^{KO}* mice.

Discussion

The study of pulmonary vascular remodeling has been limited by disease heterogeneity due to polygenic contributions. Monogenic diseases such as LAM offer a unique opportunity to study the role of specific signaling pathways on the initiation and progression of vascular remodeling. However, as vascular ECs from LAM lungs do not harbor mutations, it was previously unclear how mesenchymal LAM cells with constitutive mTORC1 hyperactivation altered EC function and could contribute to vascular remodeling. Using human LAM samples and a murine model, our study identifies cell crosstalk in the LAM lung by demonstrating that hyperactive mTORC1 mesenchyme orchestrated transcriptomic and functional changes in ECs. This contributed to the development of pulmonary vascular remodeling through paracrine stimulation of ECs by *TSC2*-null LAM mesenchymal cells. In the presence of hyperactivated mesenchymal mTORC1, vascular ECs from LAM lungs exhibited EC dysfunction characterized by altered proliferation, migration, and angiogenesis. This data suggests that EC reprogramming in LAM occurs due to paracrine ligand production by mesenchymal cells and receptor activation on ECs defining a novel mesenchyme-EC axis in the LAM lung. Moreover, parallel to the development of PH in a subset of patients with late-stage LAM, mesenchymal mTORC1 hyperactivation in aged *Tbx4*^{LME-Cre}*Tsc2*^{fl/fl} mice led to spontaneous development of pulmonary vascular remodeling highlighting the pathogenic importance of mTORC1 activation in the mesenchyme-EC axis.

Our study adds to emerging evidence that mTOR signaling contributes to the development of pulmonary vascular remodeling through pulmonary vascular cell proliferation, vasoconstriction, and chronic hypoxia (15). To date, much of the existing evidence for the effect of aberrant mTOR signaling on pulmonary vascular remodeling is limited to experimental murine models and in vitro studies utilizing primary pulmonary vascular cells. Our research focused on ECs due to their crucial role in PH initiation and progression, whereas previous studies on mTORC1 activation and pulmonary vascular remodeling have largely focused on PASMC (37, 38), where reduced *TSC2* in PASMC is associated with hyperproliferation, remodeling, and PH (39). Recent research on pulmonary vascular remodeling suggests a phenotype shift in PASMCs from contractile to synthetic phenotypes as well as skewed cellular interaction in PH samples, with most cellular interactions shifted towards smooth muscle cells

and fibroblasts (40). However, ECs have been shown to play a crucial role in pulmonary vascular remodeling through alterations in vascular tone, metabolism, oxidative stress, cell growth, and differentiation (41). Moreover, ECs can trigger PASMC proliferation through paracrine signaling (42). In our study, we found that ECs are both transcriptomically and functionally altered in the presence of hyperactive mTORC1 mesenchymal populations.

This phenomenon may not be unique to LAM, as it has been observed that primary pulmonary ECs isolated from PH patients are hyperproliferative with increased migration but reduced angiogenic capacity on standard angiogenesis assays (25, 26). However, how these ECs are affected by other pulmonary cell types and paracrine ligand-receptor signaling remains unclear. Specifically, it is unclear whether this pattern of hyperproliferative potential but reduced angiogenic capacity is a true feature of ECs or whether this is secondary to limitations of in vitro assays where ECs are neither exposed to the paracrine signaling nor experiencing biomechanical forces from the pulmonary extracellular matrix. To determine the effects of support cells and biochemical forces on the angiogenic capacity of LAM ECs, we developed EC-fibroblast cocultures to interrogate cell-cell interactions and 3D EC-fibroblast cocultures to investigate cell-matrix interactions. We found that LAM ECs, when cocultured with fibroblasts, had significantly enhanced growth and significantly altered cellular segregation, with further augmentation of EC tube length in 3D matrix models.

To further understand the mechanisms of endothelial dysfunction in an mTORC1 hyperactivated mesenchymal state, we utilized a murine model of selective mTORC1 activation in pulmonary progenitor mesenchymal cells. In *Tbx4*^{LME-Cre}*Tsc2*^{KO} mice, we showed that transcriptomic upregulation of metabolic, growth factor and angiogenic genes in ECs occurred by 8 weeks of age before phenotypic or histopathological changes were observed. However, ECs isolated from *Tbx4*^{LME-Cre}*Tsc2*^{KO} mice at these ages were functionally altered by exposure to constitutively activated mTORC1 in pulmonary mesenchyme. In fact, *Tbx4*^{LME-Cre}*Tsc2*^{KO} mice did not exhibit spontaneous pulmonary vascular remodeling with elevated right heart pressures and right ventricular hypertrophy until 1 year of age. Intriguingly, this is comparable to a human age of ~40-50 years (43, 44), the average age of respiratory failure in patients with LAM requiring initiation of the allosteric mTOR inhibitor rapamycin (Sirolimus) (45).

In addition, the mild to modest hemodynamic alteration observed in the murine model mirrors the mild PH in patients with LAM (7). As such, the development of spontaneous vascular remodeling in our aged transgenic mice is analogous to the development of PH in end-stage LAM disease and provides a mechanistic link between constitutive mesenchymal mTORC1 activation and the development of pulmonary vascular remodeling.

The presence of transcriptomic changes prior to the onset of pulmonary vascular remodeling in our murine model offered a unique opportunity to study ECs in a pre-disease state and highlights the importance of EC subpopulations. Next generation sequencing allowed us to characterize mechanistic pathways in an agnostic fashion, leading to the identification of the WNT/ β -catenin pathway as an activator of EC dysfunction in the presence of mesenchymal mTORC1 activation. Transcriptomic profiling of pulmonary cellular populations in PH is notable for EC heterogeneity (46). Different EC clusters revealed changes in cell regulation essential for the pathogenesis of PH, including upregulation of EIF2 and mTORC1 signaling (47). We identified the WNT ligand, WNT2, as a Wnt pathway signaling protein expressed by LAM mesenchyme. The canonical Wnt pathway is known to determine the vasculogenic fate of post-natal mesenchymal stem cells (48) with EC differentiation (49) and angiogenesis (50) contingent on WNT/ β -catenin signaling. Within the lung, Wnt signaling has been demonstrated to regulate the microvascular niche and drive adaptive angiogenesis in response to injury (51). We showed here that WNT inhibition limited proliferation, migration, and angiogenesis of ECs from LAM lung. The signaling between ECs and fibroblasts in cocultures was inhibited by blocking either WNT/ β -catenin or mTORC1 signaling. Lastly, WNT2 activation of ECs from control human lung elicited a LAM-like phenotype in vitro, characterized by increased cell number and altered cellular morphology. These findings confirmed the importance of the WNT pathway in pulmonary EC function and highlight the therapeutic potential of WNT pathway targets.

Taken together, our research demonstrates that mesenchymal cells with hyperactive mTORC1 activity drive EC dysfunction in LAM and in a murine model of mesenchymal mTORC1 activation. Recent research indicates complexity and heterogeneity of ECs in the pulmonary vasculature (42). Further studies are needed to delineate the significance of specific EC and mesenchymal subpopulations

involved in EC dysfunction, their responses to physiological and pathological stimuli, and their contributions to pulmonary vascular homeostasis in health and disease. Our study in LAM and the murine model of targeted *Tsc2* deletion in the lung mesenchymal cells highlights paracrine activation of receptors on ECs and reprogramming of EC functions demonstrating the prominent pathogenic importance of this cell-cell communication axis. This may have wider implications for human health as a growing body of literature has suggested that mTOR has an important role in the pathogenesis of pulmonary diseases including pulmonary arterial hypertension (15, 17-19), chronic obstructive pulmonary disease (52), and idiopathic pulmonary fibrosis (53, 54).

Methods

Experimental animals

All animal procedures were approved by the University of Pennsylvania Institutional Animal Care and Use Committee and conform to NIH guidelines on animal care. As previously described (14), *Tsc2*^{loxP/loxP} mice (55) were crossed with *Tbx4*^{LME-Cre} mice (36).

Mouse lung histology and morphometry preparation

Lungs were inflated under constant pressure (25 cm H₂O) and the pulmonary circulation was flushed with 2 cc of PBS as described (14, 56).

Human lung tissue

Normal lung samples were obtained through the University of Pennsylvania Lung Biology Institute's Human Lung Tissue Bank. These samples were obtained from deceased donors and represent secondary use of tissue. Lymphangioleiomyomatosis (LAM) lung samples were obtained from living donors at the time of lung transplantation through the National Disease Research Institute (NDRI, Philadelphia Pennsylvania). Informed consent was obtained by NDRI prior to acceptance of tissue donation for research. For both normal and diseased (LAM) lung samples, identifying information was removed prior to use in accordance with institutional and NIH protocols.

Tissue and scRNA-seq sample preparation

Lung parenchymal tissue preparation and scRNA-seq sample preparation were performed as previously described (23, 24). In brief, human lungs specimens were first confirmed to be from the most distal portion of the lung through direct visualization of the pleural lining. The pleural lining was separated from the lung parenchyma and discarded followed by microdissection along the bronchovascular tree. Specimens were then mechanically minced prior to enzymatic digestion with collagenase, dispase and DNase. Samples were then filtered, RBC lysed with ACK lysis buffer and processed into single cell suspension. CD45+ immune cells were depleted using MACS LS columns with CD45-microbeads (Miltenyi, 130-045-801) with 2×10^6 cells per column to enhance purity and viability. Following single cell suspension, the samples were loaded onto a GemCode instrument (10x Genomics) to generate single cell barcoded droplets (GEMs) according to the manufacture's protocol.

Immunohistochemistry

Human and murine paraffin-embedded tissue sections used for the immunohistochemistry experiments were sectioned and deparaffinized in xylene followed by isopropanol dilutions. Antigen retrieval was performed with 10 mM sodium citrate buffer (10 mM sodium citrate, 0.05% Tween 20, pH 6.0) following staining with primary antibodies at 4°C overnight. Secondary antibodies were incubated for 60 min at room temperature (22–24°C). Slides were mounted with Faramount Aqueous Mounting Media (Cat. No. S3025, Dako). See supplemental for primary and secondary antibodies used.

RNA Scope assay

Human paraffin-embedded tissue sections were deparaffinized in xylene followed by Ethanol dilutions and proceed to RNA Scope protocol. Target mRNA was detected using RNA Scope™ Multiplex Fluorescent Reagent Kit v2 (Advanced cell diagnostic, Cat. No. 323100) according to manufacturer manual. For visualization of the probe's hybridization, we used Opal 570 (SKU FP1488001KT, Akoya Biosciences) and Opal 690 (SKU: FP1497001KT, Akoya Biosciences) fluorophores. Images were captured on Nikon Eclipse 2000 microscope and Leica Stellaris 5 laser confocal microscope.

RNA Scope analysis

To obtain average ratio of RNA Scope probe copy to cell, we analyzed 10 images from each sample. Images were analyzed using the analyze particles plugin on Fiji 1.53.t software. Minimal and maximal particle size for the plugin was obtained by the direct measurements of both the RNA Scope fluorescent probe spot minimal size and range of nuclei size. Numbers of RNA Scope probe copy in aggregates were counted by dividing the aggregate area by the minimal spot size. Data were normalized to control.

Morphological analysis

To quantify frequency and severity of pulmonary vascular changes in transgenic mice, whole sections of mouse lungs were stained with α -smooth muscle actin (Sigma-Aldrich, #2547) and von Willebrand factor (Dako, A0082) using standard immunohistochemical protocols. Scoring of peripheral muscularization was based on 15 randomly acquired images per mouse. Peripheral vessels were defined as those small vessels distal to the terminal, muscularized bronchioles. Using a previously described method (57), the degree of muscularization was defined by α -smooth muscle actin positivity around the vascular walls and classified as non-muscularized: < 20%, partial muscularization: 20-70%, fully muscularized: > 70%. In addition, sequential mouse lung specimens were stained with α -smooth muscle actin and von Willebrand factor with automated whole lung analysis of vasculatures performed by Visiomorph™ software (Visiopharm; Hoersholm, Denmark).

Isolation of primary ECs and fibroblasts

Single cell suspensions from distal human and whole mouse lungs were prepared using previously described methods (23, 24). Immune cells were depleted using CD45-microbeads (Miltenyi, 130-045-801) and ECs were isolated after CD31+ selection with CD31+ microbeads (Miltenyi, 130-091-935). ECs were grown on EGM2 (Lonza CC3162) on collagen-coated flasks. Fibroblast cells were derived from the CD45⁻CD31⁻ fraction that were subsequently depleted of epithelial cells using EPCAM-conjugated Dynabeads (ThermoFisher 1120D). ECs were grown to confluence and sorted a second time with CD31+ microbeads prior to experimentation in passages 2-4.

Proliferation assay

Primary cells between passages 2-4 were seeded in 96-well plates at 2.5×10^3 cells/well in 200 μ L of media with 2.5% FBS. Cells were fixed with 25% glutaraldehyde and stained with 0.05% crystal violet (C3886, Sigma-Aldrich, St. Louis, MO, USA). Cells were lysed with methanol prior to absorbance reading at 590nm. For treatments, compounds were added on the day after plating and further incubated for 48- versus 72- hours. WNT inhibitor C82 was dosed at 1 μ M (dose selected based on IC50 on control cells).

Transwell cell migration assay

Transwell inserts (8 μ m pores; Corning 353097) were transferred into 24-well plates with culture medium. Cell suspensions were added to the upper chamber then incubated at 37°C and 5% CO₂ for 20 hours. Cells were fixed with glutaraldehyde and stained with crystal violet. Images were taken on EVOS and cells/field were manually counted.

Endothelial-fibroblast coculture (on 2D monolayer)

Fibroblasts were plated on 12-well plates at 9×10^4 /well and incubated for 36 hours prior to the addition of ECs at 3×10^4 /well. Media (10% EBM + EGM2 without heparin) were changed every 2 days and the cocultures were grown for 6 additional days prior to fixation (2% PFA) and staining.

Endothelial cells in matrigel (3D spherical)

Wells within a 12-well plate were precoated with fibronectin (Thermo Fisher; #33016015). Primary endothelial cells isolated as above were collected between P2-P4 were resuspended at 5×10^3 cells in 50 μ L of EGM2 (Lonza). To each sample, 50 μ L of Matrigel were added. Each 100 μ L EC-Matrigel mixture were dispensed as a droplet onto the middle of the well. Incubated at 37°C for 30 minutes to polymerize. Prewarmed 2mL EGM2 were added to each well with media changes every 2 days..

Endothelial-fibroblast cocultures in Matrigel (3D spherical)

Wells within a 12-well plate were precoated with fibronectin (Thermo Fisher; #33016015). Primary endothelial cells and fibroblasts isolated as above were collected between P2-P4. A mixture of 5×10^3 ECs and 1.5×10^4 fibroblasts were resuspended in 50 μ L of 50% EGM2/50% DMEM. To each sample, 50 μ L of Matrigel were added. Each 100 μ L EC-fibroblast coculture + Matrigel mixture were dispensed as a

droplet onto the middle of the well. Incubated at 37°C for 30 minutes to polymerize. Prewarmed 2mL 50% EGM2/50% DMEM were added to each well with media changes every 2 days.

RNA isolation and qPCR analysis for gene expression

RNeasy Micro Kit (Qiagen) was used to isolate RNA according to the manufacturer's protocol. Determination of RNA concentration and purity was performed by optical density (OD) measurement (ratio of OD at 260 nm to OD at 280 nm is greater than 1.7) using a Nano-Drop spectrophotometer (Thermo Scientific). cDNA was synthesized Verso cDNA synthesis kit (Thermo Fisher). qPCR was performed using Fast SYBR green reagents on the QuantStudio 7 Thermocycler (Life Technologies).

Immunoblot analysis

Cells were washed with DPBS prior to lysis on ice for 15 mins in RIPA cell lysis buffer (Sigma) supplemented with protease and phosphatase inhibitors (Roche) as described (14, 58). Samples were separated by SDS PAGE, transferred to nitrocellulose, blocked and incubated overnight at 4 °C with the diluted primary antibody. Blots were washed then incubated for 1 hour at RT with the appropriate LiCor secondary antibody. Image acquisition and band intensity quantification were performed using an Odyssey IR imaging system (LiCor Biosciences Lincoln, NE). Primary antibodies against TSC2, β -actin and pS6 were from Cell Signaling.

Analysis of scRNA-seq data

Reads were aligned using STARsolo v2.7.9a. For further processing, integration and downstream analysis, Seurat v.4 was used. Cells that express less than 500 genes and/or genes greater than 2 Median absolute deviation above the median were filtered out. Cells that had greater than 10% mitochondrial counts were also removed. The cell cycle phase score was calculated using CellCycleScoring function in Seurat and data was normalized and scaled using the SCTransform function, regressing out the effects of cell cycle, percent mitochondria, number of UMI per cell and number of features per cell.

Integration of the individual samples were performed using the normalized counts from SCTransform and the top 3000 variable genes as anchors. Linear dimension reduction was done using PCA, and the number of PCA dimensions was evaluated and selected based on the assessment of the ElbowPlot. Data was clustered using the Louvain graph-based algorithm in Seurat at an appropriate cluster resolution. The Uniform Manifold Approximation and Projection (UMAP) dimension reduction algorithm was used to project the cells onto a two-dimensional space for visualization. The cellular compartments (endothelium, epithelium, mesenchyme and immune) were identified using known canonical marker genes. Following compartment identification, the endothelial and mesenchymal clusters were subsetted out and the clustering and dimension reduction steps were repeated. The cell populations were then identified and annotated using either known canonical marker genes or by the assessment of the cluster-defining genes based on differential expression using the FindMarkers function in SeuratV4. GO analysis was performed using the ClusterProfiler package in R. The intercellular network analysis was performed using the CellChat v1.6.1. The minimum cell count for filtering was set at 10 and only cell populations of interest were selected for the analysis.

Hemodynamic measurements (right heart catheterization)

Hemodynamic studies were performed by the Rodent Cardiovascular Phenotyping Core (RRID: SCR_022419) at the University of Pennsylvania. The mice were anesthetized with inhalation of isoflurane 2%. The right lateral neck was dissected to isolate the right internal jugular vein. A high-fidelity pressure catheter (Millar SPR671NR) was introduced into the right internal jugular vein and passed into the right ventricle for intraventricular arterial pressure monitoring. Right ventricular systolic pressure (RVSP), end diastolic pressure (EDP), heart rate, dP/dt were recorded and analyzed using a PowerLab 10 (AD Instruments, Colorado Springs, CO, USA). After data acquisition, the pressure catheter was removed, and the animals were euthanized.

Measurement of RV hypertrophy (Fulton Index)

Hearts were excised and the RV free wall was dissected along the interventricular septum. RV hypertrophy was calculated as the weight ratio of the RV free wall relative to the left ventricle + septum (RV/LV + S). Measurements were captured using wet weights as well as dry weights with the latter obtained after specimens were dehydrated at 55°C overnight.

Statistical analysis

Statistical analyses were performed in GraphPad Prism 9. A two-tailed Student's *t*-test was used for the comparison between two experimental groups with Shapiro-Wilk test for normality. For experiments with more than two groups, a nonparametric Kruskal-Wallis ANOVA test was performed with Siegel (Bonferroni) correction for post-hoc, pair-wise contrasts. Statistical data were considered significant when $P < 0.05$.

Study Approval

All mouse experiments were performed under the protocols approved by the guidance of the University of Pennsylvania Institutional Animal Care and Use Committee (Philadelphia, PA). Human LAM specimens were obtained from the National Disease Research Interchange (Philadelphia, PA) at the time of lung transplantation through established protocols. The normal human samples used in this study were from de-identified non-used lungs donated for research (PROPEL, approved by University of Pennsylvania Institutional Review Board) with informed consent in accordance with institutional and NIH procedures. Consent was provided by next of kin or healthcare proxy and all patient information was removed before use. This use does not meet the current NIH definition of human subject research, but all institutional procedures required for human subject research were followed throughout the reported experiments.

Data availability

Murine lung scRNA-seq data that support the findings of this study have been deposited to the public functional genomics data repository Gene Expression Omnibus (GEO). Dataset available via accession ID GSE249634. Any remaining data supporting the results of the study will be made available from the corresponding author upon reasonable request.

Materials availability

All unique human and mouse lung cell lines generated in this study are available from the lead contact under material transfer request.

Author Contributions:

SML designed and performed experiments, developed 2D and 3D ECs cocultures systems, performed IHC/IF, collected and measured Fulton Index, interpreted the data, and wrote the manuscript. RR assisted with mouse care as well as mouse lung isolation. SML, MCB, LTF, JDP and EC provided access to human samples. AG, CS and OL assisted with cell culture experiments. SC assisted with hemodynamic measurements and with GK performed Visiomorph analysis. KO processed mouse lung for bulk RNA sequencing and assessed vessel wall thickness. AM performed multiple channel immunohistochemical and the RNAscope staining, image acquisition and analysis. KSV designed qPCR primers and performed the RT-PCR experiments. JFE performed western blot analysis and assisted with writing the manuscript. VPK designed the study, interpreted the data, wrote the manuscript, and directed the project.

Acknowledgements:

We thank the patients who contributed to this study, without which this study would not be possible. In addition, we thank the staff at the Rodent Cardiovascular Phenotyping Core for assistance with cardiac/hemodynamic measurements, the Pathology Core Laboratory at the Children's Hospital of Philadelphia Research Institute and the Comparative Pathology Core at the University of Pennsylvania's Veterinary School for providing histology services, and the National Disease Research Institute (NDRI, Philadelphia Pennsylvania) for providing human LAM lung explanted tissue specimens.

The authors would like to thank Dr. Michael Beers, Dr. Steve Albelda, Dr. Nilam Mangalmurti, Dr. Jacob Brenner, and Dr. Andy Vaughn for helpful discussion of the data. We would also like to thank Kevin Clark for his assistance in generating the schematic for EC isolation.

This work was supported by grants from the National Institutes of Health including F32HL162425 (SML), 5T32HL007586-35 (SML, MCB, JDP), KL2TR001879 (SML and LTF), K08HL163398 (MCB) R03HL135227 (EC), R01HL151467, R01 HL158737, R01 HL141462, R41 HL156767, U01 HL131022, DOD TSCRW W81XWH2210503 (VPK). SC was supported by the European Respiratory Society Long Term Fellowship LTRF201801-00308.

References

1. Harari S, Torre O, and Moss J. Lymphangioleiomyomatosis: what do we know and what are we looking for? *Eur Respir Rev*. 2011;20(119):34-44.
2. Henske EP, Jóźwiak S, Kingswood JC, Sampson JR, and Thiele EA. Tuberous sclerosis complex. *Nat Rev Dis Primers*. 2016;2:16035.
3. Henske EP, and McCormack FX. Lymphangioleiomyomatosis — a wolf in sheep's clothing. *Journal of Clinical Investigation*. 2012;122(11):3807-16.
4. Krymskaya VP, and McCormack FX. Lymphangioleiomyomatosis: A Monogenic Model of Malignancy. *Annu Rev Med*. 2017;68:69-83.
5. McCarthy C, Gupta N, Johnson SR, Yu JJ, and McCormack FX. Lymphangioleiomyomatosis: pathogenesis, clinical features, diagnosis, and management. *Lancet Respir Med*. 2021;9(11):1313-27.
6. McCormack FX, Gupta N, Finlay GR, Young LR, Taveira-Dasilva AM, Glasgow CG, et al. Official American Thoracic Society/Japanese Respiratory Society Clinical Practice Guidelines: Lymphangioleiomyomatosis Diagnosis and Management. *American Journal of Respiratory and Critical Care Medicine*. 2016;194(6):748-61.
7. Cottin V, Harari S, Humbert M, Mal H, Dorfmueller P, Jaïs X, et al. Pulmonary hypertension in lymphangioleiomyomatosis: characteristics in 20 patients. *Eur Respir J*. 2012;40(3):630-40.
8. Freitas CSG, Baldi BG, Jardim C, Araujo MS, Sobral JB, Heiden GI, et al. Pulmonary hypertension in lymphangioleiomyomatosis: prevalence, severity and the role of carbon monoxide diffusion capacity as a screening method. *Orphanet J Rare Dis*. 2017;12(1):74.
9. Taveira-DaSilva AM, Hathaway OM, Sachdev V, Shizukuda Y, Birdsall CW, and Moss J. Pulmonary artery pressure in lymphangioleiomyomatosis: an echocardiographic study. *Chest*. 2007;132(5):1573-8.
10. Goncharova EA, Goncharov DA, Eszterhas A, Hunter DS, Glassberg MK, Yeung RS, et al. Tuberin regulates p70 S6 kinase activation and ribosomal protein S6 phosphorylation. A role for the TSC2 tumor suppressor gene in pulmonary lymphangioleiomyomatosis (LAM). *J Biol Chem*. 2002;277(34):30958-67.
11. Kim J, and Guan KL. mTOR as a central hub of nutrient signalling and cell growth. *Nat Cell Biol*. 2019;21(1):63-71.
12. Kwiatkowski DJ, Zhang H, Bandura JL, Heiberger KM, Glogauer M, el-Hashemite N, and Onda H. A mouse model of TSC1 reveals sex-dependent lethality from liver hemangiomas, and up-regulation of p70S6 kinase activity in Tsc1 null cells. *Hum Mol Genet*. 2002;11(5):525-34.
13. Carsillo T, Astrinidis A, and Henske EP. Mutations in the tuberous sclerosis complex gene TSC2 are a cause of sporadic pulmonary lymphangioleiomyomatosis. *Proc Natl Acad Sci U S A*. 2000;97(11):6085-90.
14. Obratsova K, Basil MC, Rue R, Sivakumar A, Lin SM, Mukhitov AR, et al. mTORC1 activation in lung mesenchyme drives sex- and age-dependent pulmonary structure and function decline. *Nature Communications*. 2020;11(1).
15. Goncharov DA, Kudryashova TV, Ziai H, Ihida-Stansbury K, DeLisser H, Krymskaya VP, et al. Mammalian target of rapamycin complex 2 (mTORC2) coordinates pulmonary artery smooth muscle cell metabolism, proliferation, and survival in pulmonary arterial hypertension. *Circulation*. 2014;129(8):864-74.
16. Goncharova EA. mTOR and vascular remodeling in lung diseases: current challenges and therapeutic prospects. *Faseb j*. 2013;27(5):1796-807.
17. He Y, Zuo C, Jia D, Bai P, Kong D, Chen D, et al. Loss of DP1 Aggravates Vascular Remodeling in Pulmonary Arterial Hypertension via mTORC1 Signaling. *Am J Respir Crit Care Med*. 2020;201(10):1263-76.
18. Houssaini A, and Adnot S. mTOR: A Key to Both Pulmonary Vessel Remodeling and Right Ventricular Function in Pulmonary Arterial Hypertension? *Am J Respir Cell Mol Biol*. 2017;57(5):509-11.
19. Tang H, Wu K, Wang J, Vinjamuri S, Gu Y, Song S, et al. Pathogenic Role of mTORC1 and mTORC2 in Pulmonary Hypertension. *JACC Basic Transl Sci*. 2018;3(6):744-62.
20. Aghamohammadzadeh R, Zhang YY, Stephens TE, Arons E, Zaman P, Polach KJ, et al. Up-regulation of the mammalian target of rapamycin complex 1 subunit Raptor by aldosterone induces abnormal pulmonary artery smooth muscle cell survival patterns to promote pulmonary arterial hypertension. *Faseb j*. 2016;30(7):2511-27.
21. Pena A, Kobir A, Goncharov D, Goda A, Kudryashova TV, Ray A, et al. Pharmacological Inhibition of mTOR Kinase Reverses Right Ventricle Remodeling and Improves Right Ventricle Structure and Function in Rats. *Am J Respir Cell Mol Biol*. 2017;57(5):615-25.
22. Koslow M, Lynch DA, Cool CD, Groshong SD, and Downey GP. Lymphangioleiomyomatosis and Other Cystic Lung Diseases. *Immunol Allergy Clin North Am*. 2023;43(2):359-77.

23. Basil MC, Cardenas-Diaz FL, Kathiriya JJ, Morley MP, Carl J, Brumwell AN, et al. Human distal airways contain a multipotent secretory cell that can regenerate alveoli. *Nature*. 2022;604(7904):120-6.
24. Zacharias WJ, Frank DB, Zepp JA, Morley MP, Alkhaleel FA, Kong J, et al. Regeneration of the lung alveolus by an evolutionarily conserved epithelial progenitor. *Nature*. 2018;555(7695):251-5.
25. Masri FA, Xu W, Comhair SA, Asosingh K, Koo M, Vasanji A, et al. Hyperproliferative apoptosis-resistant endothelial cells in idiopathic pulmonary arterial hypertension. *Am J Physiol Lung Cell Mol Physiol*. 2007;293(3):L548-54.
26. Tura-Ceide O, Smolders VFED, Aventin N, Morén C, Guitart-Mampel M, Blanco I, et al. Derivation and characterisation of endothelial cells from patients with chronic thromboembolic pulmonary hypertension. *Scientific Reports*. 2021;11(1).
27. Guo M, Morley MP, Jiang C, Wu Y, Li G, Du Y, et al. Guided construction of single cell reference for human and mouse lung. *Nat Commun*. 2023;14(1):4566.
28. Sun X, Perl A-K, Li R, Bell SM, Sajti E, Kalinichenko VV, et al. A census of the lung: CellCards from LungMAP. *Developmental Cell*. 2022;57(1):112-45.e2.
29. Travaglini KJ, Nabhan AN, Penland L, Sinha R, Gillich A, Sit RV, et al. A molecular cell atlas of the human lung from single-cell RNA sequencing. *Nature*. 2020;587(7835):619-25.
30. Zepp JA, and Morrissey EE. Cellular crosstalk in the development and regeneration of the respiratory system. *Nat Rev Mol Cell Biol*. 2019;20(9):551-66.
31. Schupp JC, Adams TS, Cosme C, Jr., Raredon MSB, Yuan Y, Omote N, et al. Integrated Single-Cell Atlas of Endothelial Cells of the Human Lung. *Circulation*. 2021;144(4):286-302.
32. Zepp JA, Zacharias WJ, Frank DB, Cavanaugh CA, Zhou S, Morley MP, and Morrissey EE. Distinct Mesenchymal Lineages and Niches Promote Epithelial Self-Renewal and Myofibrogenesis in the Lung. *Cell*. 2017;170(6):1134-48.e10.
33. de Jesus Perez V, Yuan K, Alastalo TP, Spiekerkoetter E, and Rabinovitch M. Targeting the Wnt signaling pathways in pulmonary arterial hypertension. *Drug Discov Today*. 2014;19(8):1270-6.
34. Evans JF, Obratzsova K, Lin SM, and Krymskaya VP. CrossTORC and WNTegration in Disease: Focus on Lymphangioleiomyomatosis. *Int J Mol Sci*. 2021;22(5).
35. Zhou H, Mak PY, Mu H, Mak DH, Zeng Z, Cortes J, et al. Combined inhibition of β -catenin and Bcr-Abl synergistically targets tyrosine kinase inhibitor-resistant blast crisis chronic myeloid leukemia blasts and progenitors in vitro and in vivo. *Leukemia*. 2017;31(10):2065-74.
36. Kumar ME, Bogard PE, Espinoza FH, Menke DB, Kingsley DM, and Krasnow MA. Mesenchymal cells. Defining a mesenchymal progenitor niche at single-cell resolution. *Science*. 2014;346(6211):1258810.
37. Deng H, Hershenson MB, Lei J, Anyanwu AC, Pinsky DJ, and Bentley JK. Pulmonary artery smooth muscle hypertrophy: roles of glycogen synthase kinase-3 β and p70 ribosomal S6 kinase. *Am J Physiol Lung Cell Mol Physiol*. 2010;298(6):L793-803.
38. Goncharova EA, Ammit AJ, Irani C, Carroll RG, Eszterhas AJ, Panettieri RA, and Krymskaya VP. PI3K is required for proliferation and migration of human pulmonary vascular smooth muscle cells. *Am J Physiol Lung Cell Mol Physiol*. 2002;283(2):L354-63.
39. Shen Y, Goncharov DA, Pena A, Baust J, Chavez Barragan A, Ray A, et al. Cross-talk between TSC2 and the extracellular matrix controls pulmonary vascular proliferation and pulmonary hypertension. *Sci Signal*. 2022;15(763):eabn2743.
40. Crnkovic S, Valzano F, Fließner E, Gindlhuber J, Thekkekara Puthenparampil H, Basil M, et al. Single-cell transcriptomics reveals skewed cellular communication and phenotypic shift in pulmonary artery remodeling. *JCI Insight*. 2022;7(20).
41. Evans CE, Cober ND, Dai Z, Stewart DJ, and Zhao YY. Endothelial cells in the pathogenesis of pulmonary arterial hypertension. *Eur Respir J*. 2021;58(3).
42. Eddahibi S, Guignabert C, Barlier-Mur AM, Dewachter L, Fadel E, Darteville P, et al. Cross talk between endothelial and smooth muscle cells in pulmonary hypertension: critical role for serotonin-induced smooth muscle hyperplasia. *Circulation*. 2006;113(15):1857-64.
43. Dutta S, and Sengupta P. Men and mice: Relating their ages. *Life Sci*. 2016;152:244-8.
44. Wang S, Lai X, Deng Y, and Song Y. Correlation between mouse age and human age in anti-tumor research: Significance and method establishment. *Life Sci*. 2020;242:117242.
45. Revilla-López E, Berastegui C, Méndez A, Sáez-Giménez B, Ruiz de Miguel V, López-Meseguer M, et al. Long-term results of sirolimus treatment in lymphangioleiomyomatosis: a single referral centre experience. *Sci Rep*. 2021;11(1):10171.
46. Saygin D, Tabib T, Bittar HET, Valenzi E, Sembrat J, Chan SY, et al. Transcriptional profiling of lung cell populations in idiopathic pulmonary arterial hypertension. *Pulm Circ*. 2020;10(1).

47. Asosingh K, Comhair S, Mavrakakis L, Xu W, Horton D, Taylor I, et al. Single-cell transcriptomic profile of human pulmonary artery endothelial cells in health and pulmonary arterial hypertension. *Sci Rep*. 2021;11(1):14714.
48. Zhang Z, Nör F, Oh M, Cucco C, Shi S, and Nör JE. Wnt/ β -Catenin Signaling Determines the Vasculogenic Fate of Postnatal Mesenchymal Stem Cells. *Stem Cells*. 2016;34(6):1576-87.
49. Yuan K, Orcholski ME, Panaroni C, Shuffle EM, Huang NF, Jiang X, et al. Activation of the Wnt/planar cell polarity pathway is required for pericyte recruitment during pulmonary angiogenesis. *Am J Pathol*. 2015;185(1):69-84.
50. Aros CJ, Pantoja CJ, and Gomperts BN. Wnt signaling in lung development, regeneration, and disease progression. *Commun Biol*. 2021;4(1):601.
51. Summers ME, Richmond BW, Menon S, Sheridan RM, Kropski JA, Majka SA, et al. Resident mesenchymal vascular progenitors modulate adaptive angiogenesis and pulmonary remodeling via regulation of canonical Wnt signaling. *Faseb j*. 2020;34(8):10267-85.
52. Houssaini A, Breau M, Kebe K, Abid S, Marcos E, Lipskaia L, et al. mTOR pathway activation drives lung cell senescence and emphysema. *JCI Insight*. 2018;3(3).
53. Lawrence J, and Nho R. The Role of the Mammalian Target of Rapamycin (mTOR) in Pulmonary Fibrosis. *Int J Mol Sci*. 2018;19(3).
54. Woodcock HV, Eley JD, Guillotin D, Platé M, Nanthakumar CB, Martufi M, et al. The mTORC1/4E-BP1 axis represents a critical signaling node during fibrogenesis. *Nature Communications*. 2019;10(1).
55. Hernandez O, Way S, McKenna J, 3rd, and Gambello MJ. Generation of a conditional disruption of the Tsc2 gene. *Genesis*. 2007;45(2):101-6.
56. Goncharova EA, Goncharov DA, James ML, Atochina-Vasserman EN, Stepanova V, Hong SB, et al. Folliculin controls lung alveolar enlargement and epithelial cell survival through E-cadherin, LKB1, and AMPK. *Cell Rep*. 2014;7(2):412-23.
57. Frank DB, Abtahi A, Yamaguchi DJ, Manning S, Shyr Y, Pozzi A, et al. Bone morphogenetic protein 4 promotes pulmonary vascular remodeling in hypoxic pulmonary hypertension. *Circ Res*. 2005;97(5):496-504.
58. Himes BE, Obraztsova K, Lian L, Shumyatcher M, Rue R, Atochina-Vasserman EN, et al. Rapamycin-independent IGF2 expression in Tsc2-null mouse embryo fibroblasts and human lymphangioleiomyomatosis cells. *PLoS One*. 2018;13(5):e0197105.

Results

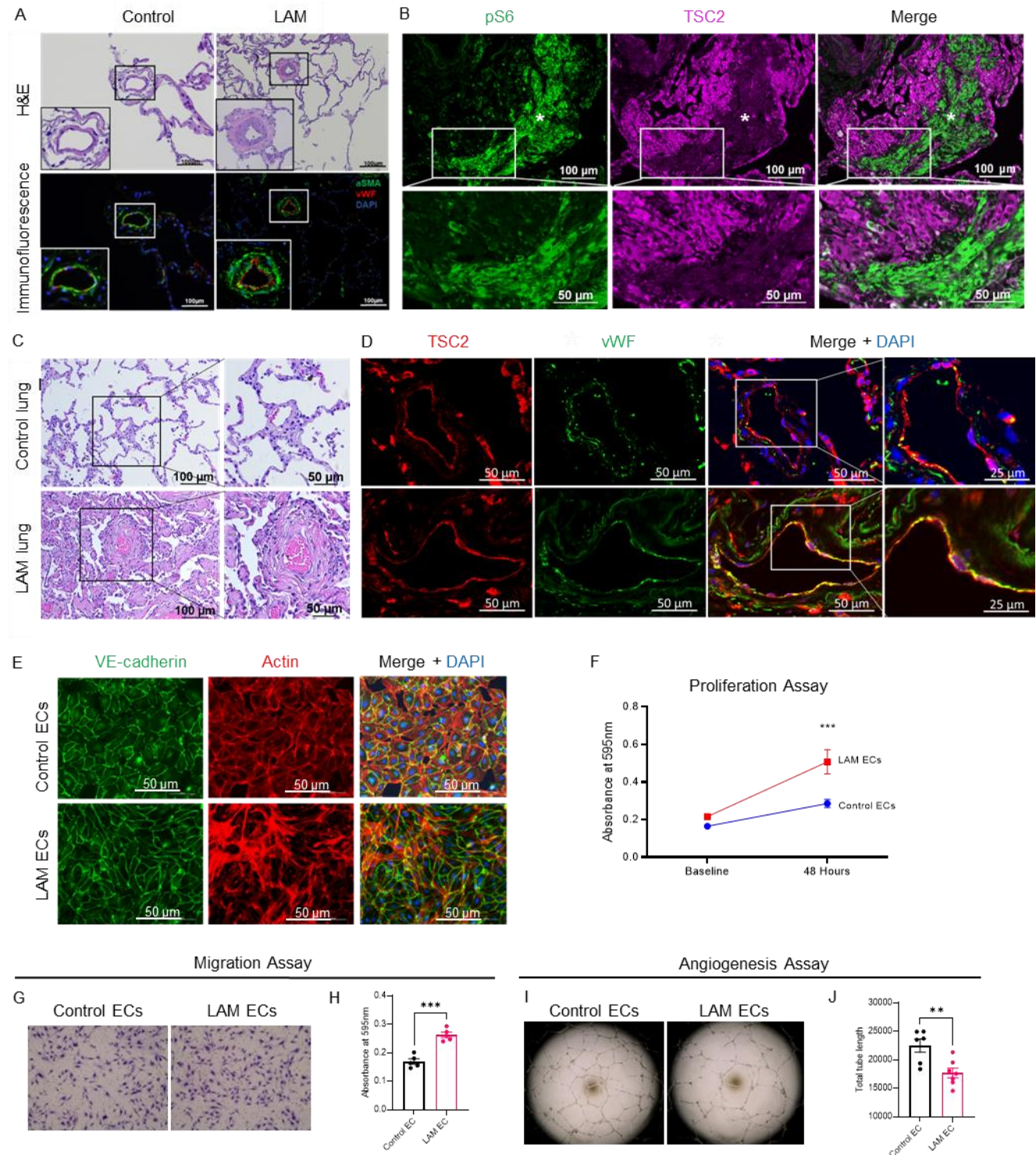


Figure 1. Characterization of pulmonary ECs from patients with LAM. Representative images of H&E and immunofluorescent-stained LAM lung (n=3) compared to age- and sex- matched control human lung (n=3) showing (A) remodeled distal vasculatures detected with antibodies against von Willebrand factor (vWF, red) and smooth muscle α -actin (α SMA, green) and (B) increased intimal fibrosis and medial thickening by H&E. DAPI detects nuclei (blue). (C) Representative images of dual immunofluorescent staining of human LAM lung (n=3) demonstrating loss of TSC2 (tuberin, magenta) expression in LAM lesion and concurrent activation of pS6 (marker of mTOR activation, green) and DAPI (nuclei; blue). *LAM micronodules. (D) Representative images of positive immunoreactivity for TSC2 protein (tuberin, magenta) and vWF (green) in ECs lining of the pulmonary vasculatures in both human control (n=4) and LAM lungs (n=4). DAPI (nuclei;

blue). (E) LAM and control pulmonary ECs labelled with antibodies against endothelial marker vWF (green) and F-actin (rhodamine phalloidin; red). Nuclei counterstained using DAPI (blue). (F) Proliferation of control and LAM ECs over 48 hours using a crystal violet growth assay. (G) Representative images of EC migration of control (n=5) and LAM EC (n=5) performed using Boyden chamber assay. (H) Statistical analysis of ECs migration quantified at 24 hours post-migration using two-tailed t tests of crystal violet absorbance; data are represented as mean \pm SEM. ** $P < 0.01$. (I) Representative image of in vitro angiogenesis in 2D of control (n=6) and LAM (n=6) ECs. (J) Total tube length at 24 hours of growth on Matrigel was analyzed using Angiogenesis Analyzer plugin on Image J, followed by statistical analysis using two-tailed t tests and data are represented as mean \pm SEM. * $P < 0.05$; ** $P < 0.01$; *** $P < 0.001$; **** $P < 0.0001$.

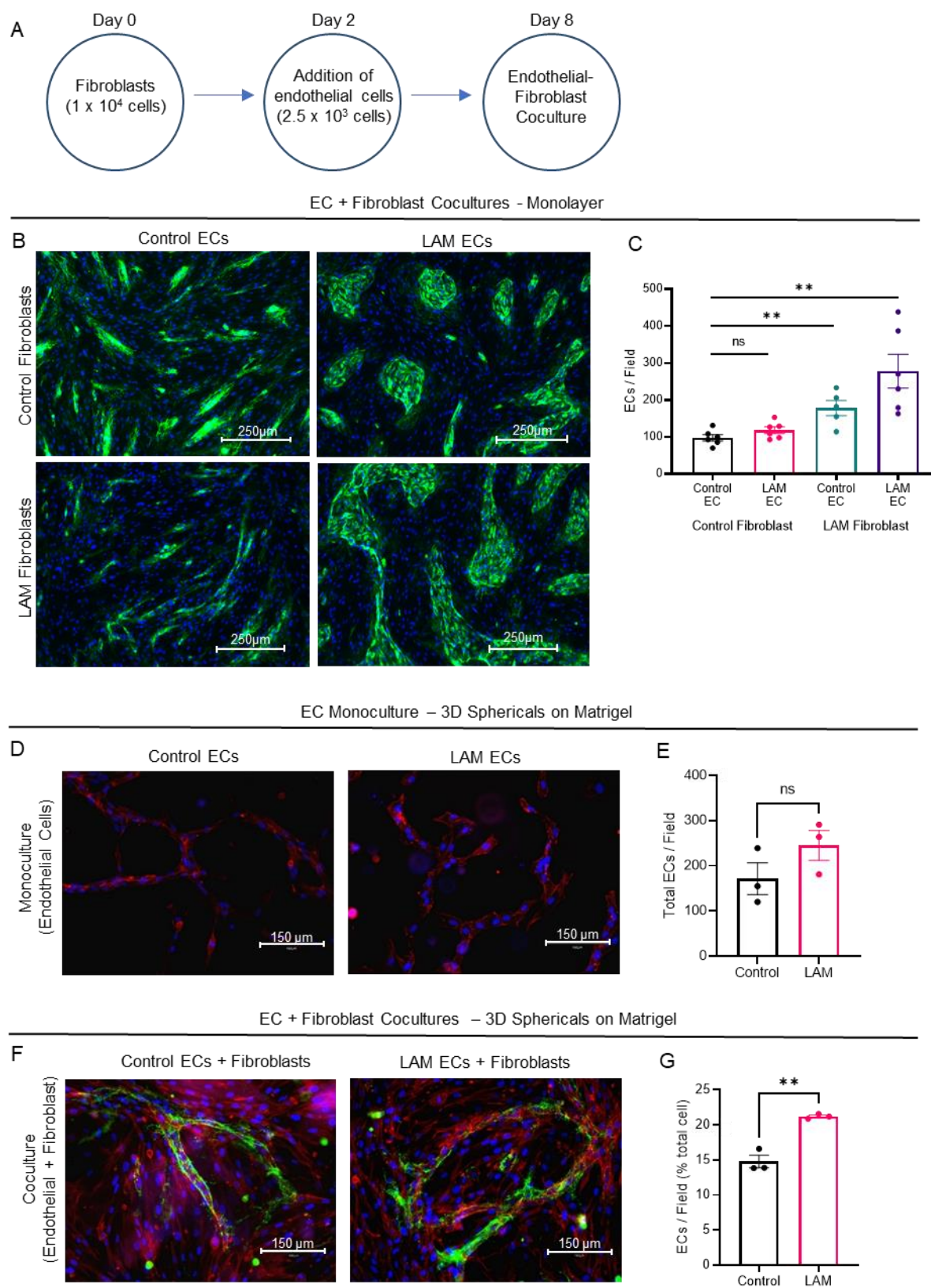


Figure 2. Increased EC proliferation and in vitro vasculogenesis in three-dimensional (3D) endothelial-fibroblast coculture systems. (A) Schematic for endothelial-fibroblast coculture experiments. (B) Representative images of endothelial-fibroblast cocultures in monolayer at day 8 using primary cells isolated from LAM lung explants and age-matched control human lung. ECs stained with vWF (green) and nuclei counterstained with DAPI (blue). Images acquired at 10x and 20x magnification. (C) Quantification of number of ECs per field in the endothelial-fibroblast cocultures. (D) Representative

images of 3D control (n=3) and LAM (n=3) EC sphericals in serum-free matrigel matrix. Cells were stained with rhodamine phalloidin (red) to visualize ECs structure. (E) Quantification of total number of ECs per field by nonparametric Kruskal-Wallis ANOVA test with Siegel (Bonferroni) correction. (F) Representative images of 3D sphericals with control (n=3) and LAM (n=3) ECs grown in the presence of fibroblasts from control human and LAM lung, respectively, on serum-free matrigel matrix. ECs were immunostained with vWF (green) and nuclei counterstained with DAPI (blue). (G) Quantification of ECs/field (% of total cells) in 3D cocultures. Statistical analysis by nonparametric Kruskal-Wallis ANOVA test with Siegel (Bonferroni) correction for post-hoc, pair-wise contrasts (C, E and G). * $P < 0.05$; ** $P < 0.01$; *** $P < 0.001$; **** $P < 0.0001$.

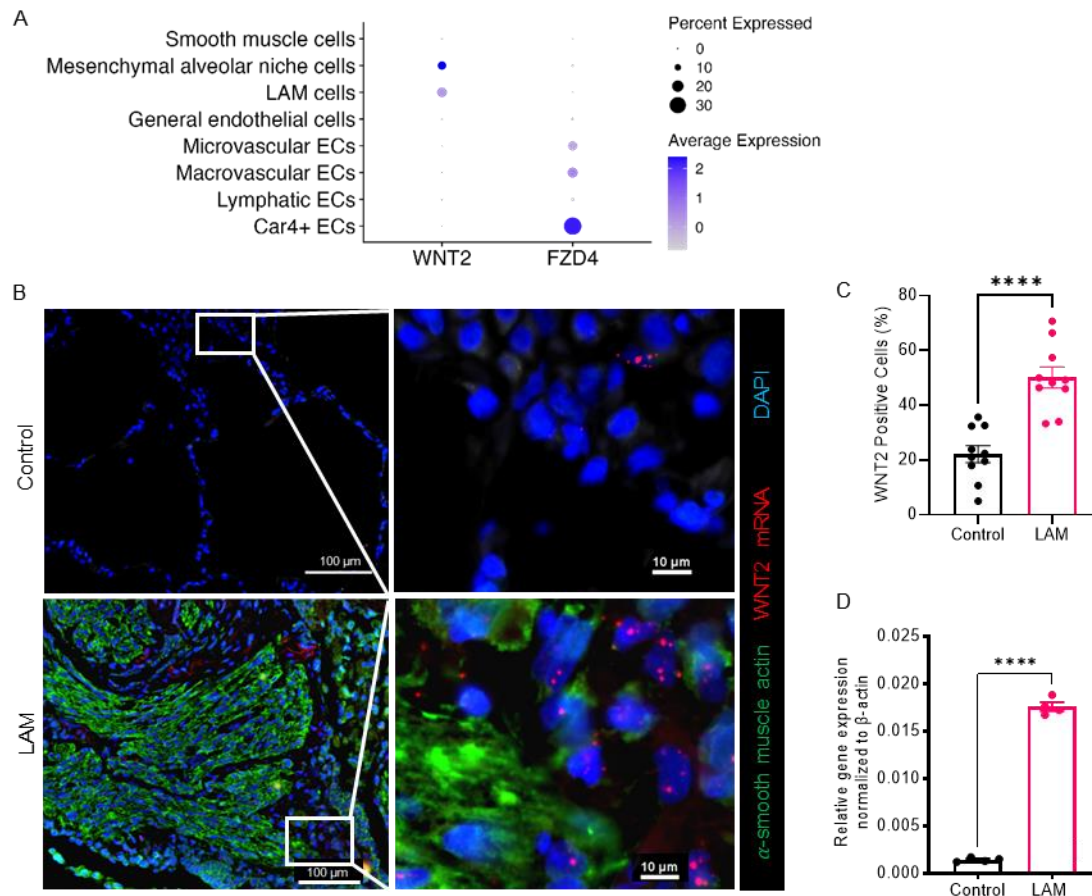


Figure 3. Identification of WNT2 in LAM lung mesenchyme. (A) Gene expression dot plot highlighting the unique expression of Wnt2 in LAM cell cluster and mesenchymal alveolar niche cell clusters with corresponding Fzd4, a WNT2 receptor, in Car4-positive (+) EC subcluster within LAM lung. (B) Representative images of dual staining with WNT2 mRNA scope (red) in situ Hybridization and α -smooth muscle actin (green) of LAM (n=3) and control human lung (n=3). DAPI (blue) detects nuclei. (C) Statistical analysis of WNT2 mRNA-positive cells in control compared to LAM lungs calculated as percentage of WNT2-positive cells per total number of cells as described in Methods. (D) Validation of WNT2 RNA transcripts on the mRNA samples isolated from the lung mesenchyme of control (n=4) and LAM lungs (n=4). The data points represent relative gene expression values normalized to the expression of β -actin gene using ddCt method. Statistical analysis was performed using the nonparametric T-test comparisons. * P<0.05; ** P<0.01; *** P<0.001; **** P<0.0001.

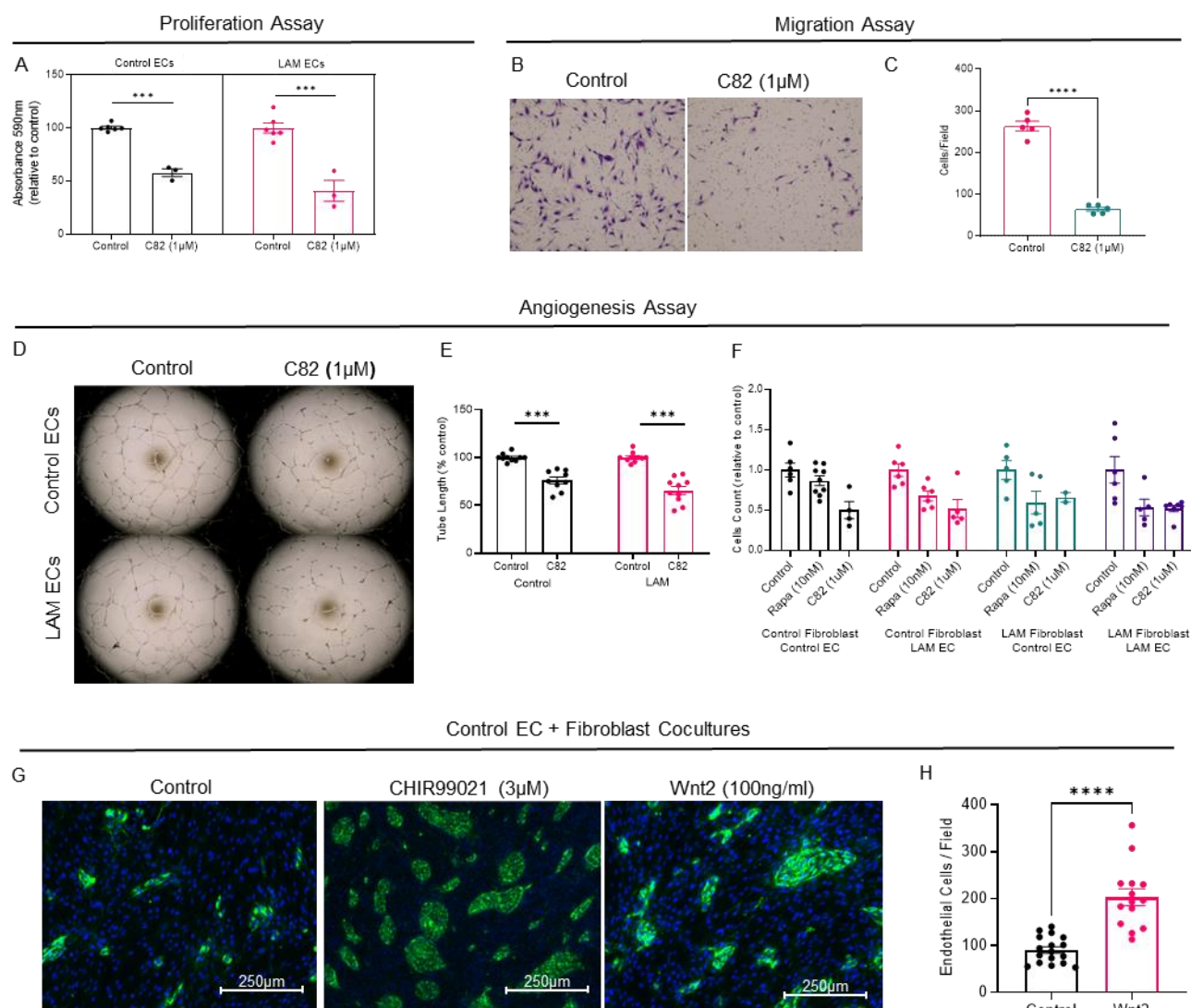


Figure 4. Inhibition of WNT suppresses EC proliferation, migration and angiogenesis. (A) Control ECs (n=6) and LAM ECs cells (n=3) were treated with 1μM WNT inhibitor C82 followed by proliferation assay as described in Methods. (B) Representative images of migration of ECs from LAM lung treated with 1uM C82 or diluent (control). (C) Statistical analysis of LAM EC migration calculated as number of cells/field in control (n=5) versus 1μM C82-treated LAM ECs (n=5). (D) Representative images from angiogenesis assay of control ECs and LAM ECs treated with diluent or 1uM C82. (E) Analysis of total tube length of control ECs compared to LAM ECs was performed using Angiogenesis Analyzer plugin on Image J followed by statistical analysis using two-tailed t tests with control condition taken as 100%. (F) Effect of 10nM rapamycin and 1μM C82 on endothelial-fibroblast cocultures. (G) Endothelial-fibroblast cocultures of control human ECs with control human lung fibroblasts were treated with diluent (control), stimulated with pan WNT pathway activator CHIR99021 (3μM), or WNT2 (100ng/ml); n=3 in each treatment group. (H) Statistical analysis of ECs per field (with minimum of 4 images per well) in cocultures treated with WNT2 were performed using two-tailed t tests and data are represented as mean ± SEM. * P<0.05; ** P<0.01; *** P<0.001; **** P<0.0001.

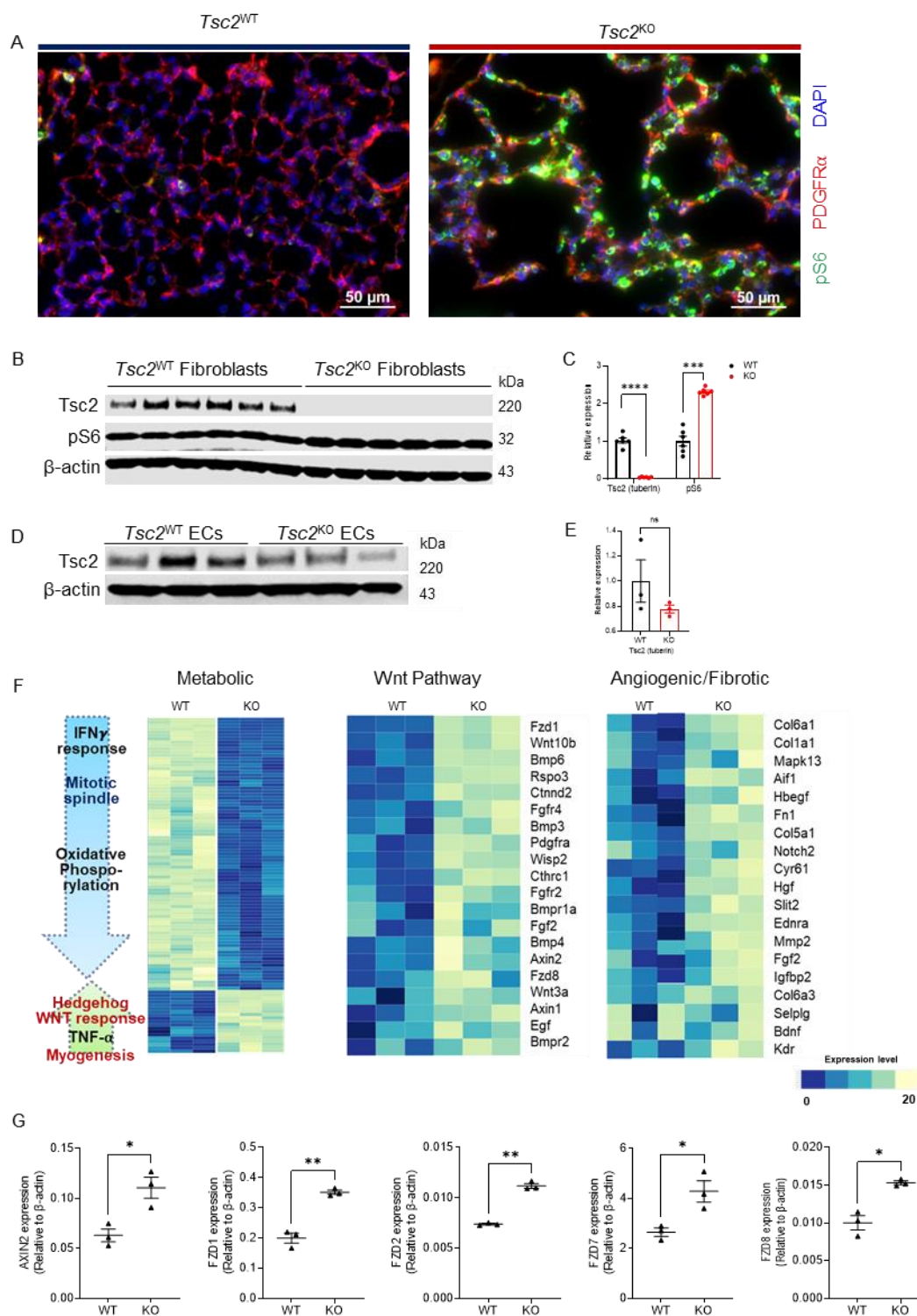


Figure 5. Differential gene expression in the CD31+ vascular ECs from *Tbx4^{LME-Cre}Tsc2^{KO}* mouse lung. (A) Representative images of immunofluorescent staining of distal lung demonstrate positivity of pS6, a marker of mTORC1 upregulation (green) in PDGFR α (red) mesenchymal cells of 8-week-old *Tbx4^{LME-Cre}Tsc2^{KO}* (*Tsc2^{KO}*) mouse lungs. (B) Immunoblot of Tsc2 and pS6 proteins expression in *Tsc2^{WT}* (n=3 in duplicates) and *Tsc2^{KO}* (n=3 in duplicates) in 12-week-old mouse lung fibroblasts. (C) Statistical analysis of densitometry of Tsc2 and pS6 levels normalized to β -actin in each lane with average levels in *Tsc2^{WT}* wild-type taken as 1. (D) Immunoblot of Tsc2 expression in lung ECs from *Tsc2^{WT}* (n=3) and *Tsc2^{KO}* (n=3) 8-week-old mice. (E) Statistical analysis of Tsc2 densitometry normalized to β -actin in each lane with the average expression levels in *Tsc2^{WT}* set as 1. (F) Heatmap of the top differentially expressed genes in the mouse lung ECs isolated from *Tsc2^{WT}* (n=3) and *Tsc2^{KO}* (n=3) mice. (G) qPCR of Wnt pathway activation Axin2, ligands and receptors in ECs

from lung of 8-week-old *Tsc2*^{WT} (n=3) and *Tsc2*^{KO} (n=3) 8-week-old mice. Statistical analysis was performed using two-tailed t tests and data are represented as mean \pm SEM. * P<0.05; ** P<0.01; *** P<0.001; **** P<0.0001.

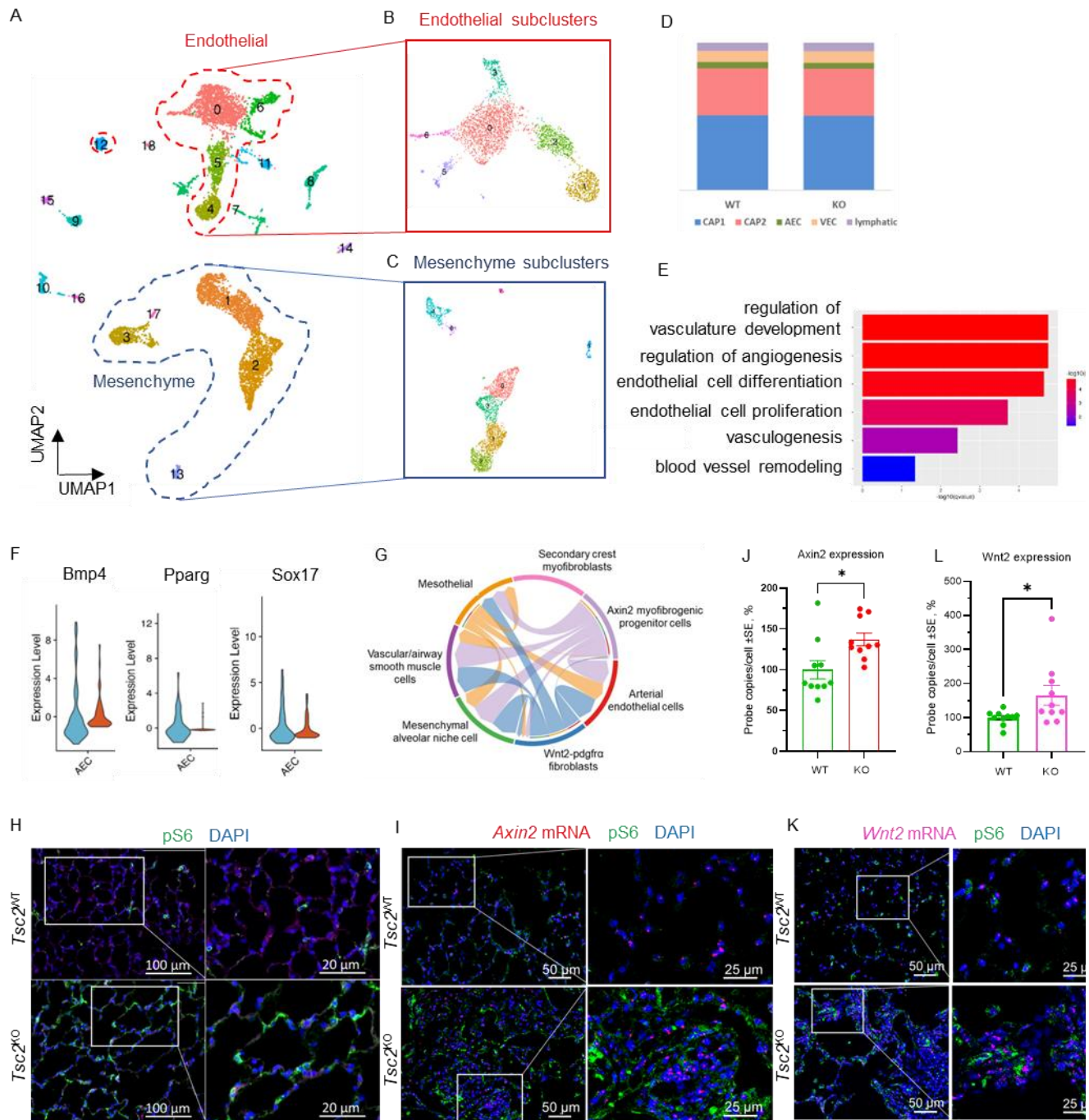


Figure 6. Transcriptomic heterogeneity of ECs in *Tbx4*^{LME-Cre}*Tsc2*^{KO} mouse lung. (A) Uniform manifold approximation and projection (UMAP) representation of *Tsc2*^{WT} and *Tsc2*^{KO} mouse lungs (n=2) scRNA-seq with cell populations labelled according to the corresponding cell type. (B) ECs, marked by *Pecam1* and *vWF* expression, were reclustered into 6 subclusters. (C) Mesenchymal cells, marked by *Pdgfra*, *Pdgfr β* and *Msln* expression, were reclustered into 8 subclusters. (D) Distribution of each EC type within the endothelial subclusters. (E) Gene Ontology (GO) enrichment analysis of arterial EC cluster. (F) WNT signaling pathway network (chord diagram) with incoming signal to arterial ECs from 3 mesenchymal populations including Axin2 myofibroblastic progenitor (AMP), Wnt2-Pdgfra cells, and mesothelial cells. (G) Violin plot demonstrating increased expression of *Bmp4*, *Pparg*, and *Sox17* in arterial (AECs) from *Tsc2*^{KO} mice compared to arterial ECs from *Tsc2*^{WT}. (H) Representative images of 54-week-old *Tsc2*^{WT} (n=3) and *Tsc2*^{KO} (n=3) for pS6 (marker of mTORC1 upregulation; magenta); light green reflects an autofluorescence from structural proteins in lung mesenchyme. DAPI (blue) detects nuclei. (I) Representative images of dual staining of 54-week-old *Tsc2*^{WT} (n=3) and *Tsc2*^{KO} (n=3) lung for *Axin2* mRNA (magenta) and pS6 (green). (J) Quantification of *Axin2* mRNA shown in (I). (K) Pulmonary vasculature in both *Tsc2*^{WT} and *Tsc2*^{KO} with *Wnt2* mRNA (magenta) and pS6 (green) from single-molecule fluorescent in situ hybridization. (L) Quantification of *Wnt2* mRNA shown in (K). Statistical analysis was performed using two-tailed t tests and data are represented as mean \pm SEM. * P<0.05; ** P<0.01; *** P<0.001; **** P<0.0001.

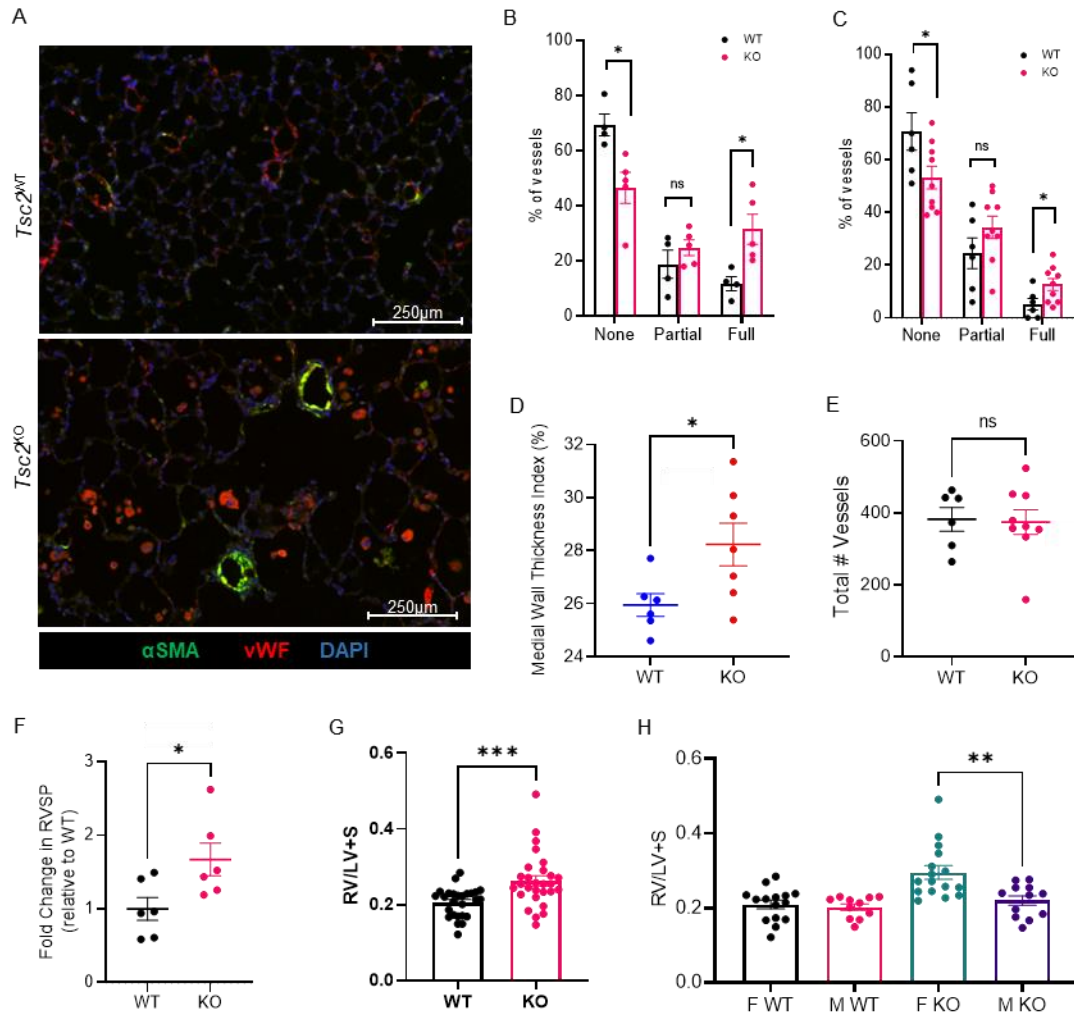


Figure 7. Pulmonary vascular remodeling and right heart dysfunction in one-year-old *Tbx4^{LME-Cre}Tsc2^{KO}* mice with mesenchymal mTOR activation. (A) Representative images of vessels in *Tsc2^{WT}* compared to *Tsc2^{KO}* in one-year-old mice. (B) Scoring of peripheral muscularization based on 15 randomly acquired images per mouse (n=9). (C) Peripheral muscularization based on automated measurements obtained on Visiomorph™. Morphometric analysis of pulmonary vascular remodeling in *Tsc2^{KO}* (n=9, red) mice compared to *Tsc2^{WT}* mice (n=6, blue). (D) Medial wall thickness based on Visiomorph. Medial wall thickness was defined as: (vessel diameter minus luminal diameter)/ 2. Comparison of *Tsc2^{WT}* (n=6) to *Tsc2^{KO}* (n=7). (E) Total number of vessels unchanged in *Tsc2^{WT}* vs *Tsc2^{KO}*. (F) Right heart catheterization of one-year-old *Tsc2^{WT}* (n=6) and *Tsc2^{KO}* (n=6) mice with comparison of RVSP in terms of fold change relative to baseline *Tsc2^{WT}* RVSP of 12.9mmHg. (G) Right ventricular hypertrophy (RVH) as measured by Fulton index (RV/S+LV); *Tsc2^{WT}* (n=25) vs *Tsc2^{KO}* (n=27). (H) Increased Fulton indices were driven by females *Tsc2^{KO}* (n=13) compared to male *Tsc2^{KO}* (n=11). Statistical analysis was performed using two-tailed t tests and data are represented as mean ± SEM. * P<0.05; ** P<0.01; *** P<0.001; **** P<0.0001.

Antibodies, reagents, and mRNA probes

Antibody	Company	Catalog #	Isotype	Conc.
(1) α -smooth muscle actin	Sigma-Aldrich	A2547	mouse	1:250
(2) PDGFR α	Cell Signaling	3174	rabbit	1:100
(3) pS6	Cell Signaling	62016	mouse	1:250
(4) VE- cadherin	Thermo Fisher	36-1900	rabbit	1:100
(5) Tuberin/TSC2 (D93F12) XP®	Cell Signaling	4308	rabbit	1:200
(6) von Willebrand factor	Abcam	ab201336	mouse	1:20
(7) von Willebrand factor	Dako	A0082	rabbit	1:100
(8) Goat Anti-Rabbit IgG H&L (Alexa Fluor® 594)	Abcam	ab150080	goat	1:250
(9) Goat Anti-Mouse IgG H&L (Alexa Fluor® 594)	Abcam	ab150116	goat	1:250
(10) Goat Anti-Rabbit IgG H&L (Alexa Fluor® 488)	Abcam	ab150077	goat	1:250
(11) Goat Anti-Mouse IgG H&L (Alexa Fluor® 488)	Abcam	ab150113	goat	1:250
(12) Goat Anti-Mouse IgG H&L (Alexa Fluor® 647)	Abcam	ab150115	goat	1:250
(13) Goat Anti-Rabbit IgG H&L (Alexa Fluor® 647)	Abcam	ab150083	goat	1:250
(14) Rhodamine Phalloidin	Thermo Fisher	R415		
(15) RNAscope® Probe- Hs-AXIN2	ACDBio	400241-C2		
(16) RNAscope® Probe- Hs-WNT2	ACDBio	584071		
(17) RNAscope™ Probe- Mm-Axin2-C2	ACDBio	400331-C2		
(18) RNAscope™ Probe- Mm-Wnt2	ACDBio	313601		